NUMERICAL STUDY OF STRONG INTERPLAY BETWEEN CAVITY AND STORE DURING LAUNCHING

P. P. Yan **Q. F. Zhang***

Department of Mechanics
School of Civil Engineering
Beijing Jiaotong University
Beijing, China

J. Li

Shenyang Aircraft Design and Research Institute
Aviation Industry of China
Shenyang, China

ABSTRACT

Numerical investigation of the strong interplay between a cavity and a store under supersonic inflow condition is conducted by using Improved Delayed Detach-Eddy Simulation (IDDES). Pressure fluctuations in the cavity are analyzed with smooth pseudo Winger-Vile distribution method and the time-frequency features are obtained. The effects of fluctuating flow inside the cavity on the aerodynamic loads of the store are also studied. It was shown that when the store is falling through the shear layer, the self-sustained oscillation loop is destroyed and the cavity tone vanishes. Vortex structures concentrate in the back of the cavity, as a result the noise levels at the rear of the cavity increase. After the store falls out of the cavity, the oblique shock wave formed at store's head interferences with the shear layer, which changes the cavity tone frequencies. The forces and moments acting on the store fluctuate strongly influenced by highly unsteady flow-field. Affected by oblique shock and the impact of shear layer, the store's pitch up angle keeps rising up and reaches to 24° at its maximum.

Keywords: IDDES, Weapon launch, Cavity noise, Smooth pseudo winger-vile distribution.

1. INTRODUCTION

The buried weapon bay system is widely used in the new generation of fighter aircrafts due to the reduction in aerodynamic drag, heating and radar cross-section [1, 2]. However, a highly unsteady and fluctuating flow field develops when the weapon is released and the cavity is exposed to the free stream, which poses a number of aerodynamic challenges, such as strong pressure fluctuations and acoustic resonance onset from a feedback loop within the cavity. Subsequently, excessive structural loading may be induced on the aircraft and eventually damage vital flight instrumentations. On the other hand, the pressure fluctuation can also deviate significantly released stores from projected trajectory [3, 4].

Since 1950s, a large volume of experimental and computational work has been devoted to investigating various aspects of cavity flow. Sun [5] found that at low Reynolds number, widening the cavity can decrease the velocity fluctuations of the flow by introducing span wise variations in the flow field. Thiemann [6] and Givogue [7] studied passive control method by placing vertical or horizontal cylinders at the cavity leading edge and found that the suppression levels were affected by shape, density and height of the cylinders. Zhang [8], Williams [9] and Thangamani [10] studied the active control method of pulsed blowing and injections from the cavity leading edge or the cavity floor, and found the suppression values were sensitive to the injection pressure and momentum. Robertson [11] studied the aero-acoustic characteristics of a supersonic cavity with a generic store by both experiments and numerical methods. His result showed that not only the resonance modes in the cavity were altered but also the energy was redistributed among various modes.

Most of the studies assume a clean cavity or a cavity with a fixed store and results on cavity-store interactions in the true dynamic separation are not directly available. As the store falls out of the weapon bay and passes through the shear layer, the flow undergoes destruction

* Corresponding author (zhangqunfeng@263.net)

DOI : 10.1017/jmech.2017.45
Copyright © 2017 The Society of Theoretical and Applied Mechanics
https://doi.org/10.1017/jmech.2017.45 Published online by Cambridge University Press

and reconstruction, which elevates the unsteadiness and noise level of the flow field. Meanwhile, the forces acting on the store change rapidly during this process and may result in unsafe separations and missing targeting. Therefore, better understanding of the strong interactions will help mitigate risks and increase target accuracy.

This paper is organized as follows. Governing equations and numerical methodology are described in the next section, which are followed by two validation cases. In the third section, the details of simulation models are present along with results and analysis in various settings. We conclude the paper with a discussion on future work.

2. METHODOLOGY

2.1 Governing Equations

For store separation problem, the modified form of the Navier-Stokes equations which accounts for the relative motion of the grid with respect to the fluid is shown as below [12],

$$\frac{\partial}{\partial t}\int_{\Omega} \boldsymbol{W} d\Omega + \oint_{\partial\Omega} (\boldsymbol{F}_c^M - \boldsymbol{F}_v) dS = \int_{\Omega} \boldsymbol{Q} d\Omega, \tag{1}$$

Where t is time, $\boldsymbol{W}$ denotes conservative variables, $\boldsymbol{F}_c^M$ represents the vector of the convective fluxes, $\boldsymbol{F}_v$ stands for the vector of viscous fluxes, $\boldsymbol{Q}$ is the source term, Ω denotes control volume, and dS represents surface element. The conservative variables

$$\boldsymbol{W} = [\rho \quad \rho u \quad \rho v \quad \rho w \quad \rho E]^T, \tag{2}$$

Where ρ, u, v, w, E denote the density, the Cartesian velocity components and the total energy per unite mass, respectively. The vector of the convective fluxes $\boldsymbol{F}_c^M$ on dynamic grids can be written as

$$\boldsymbol{F}_c^M = \begin{bmatrix} \rho V_r \\ \rho u V_r + n_x p \\ \rho v V_r + n_y p \\ \rho w V_r + n_z p \\ \rho H V_r + V_t p \end{bmatrix}, \tag{3}$$

Where V_r represents the contravariant velocity relative to the motion of the grid, p denotes static pressure, and H is total enthalpy. The relative contravariant velocity

$$V_r = V - V_t, \tag{4}$$

Where V is contravariant velocity, and V_t is the contravariant velocity of the face of the control volume. These two velocities read

$$V = \vec{U} \cdot \boldsymbol{n} = n_x u + n_y v + n_z w, \tag{5}$$

$$V_t = \boldsymbol{g} \cdot \boldsymbol{n} = n_x \frac{\partial x}{\partial t} + n_y \frac{\partial y}{\partial t} + n_z \frac{\partial z}{\partial t}, \tag{6}$$

Where $\vec{U}$ is velocity vector, $\boldsymbol{g}$ represents the grid velocity, and n_x, n_y, n_z denote the components of the outward facing unit normal vector of the surface $\partial\Omega$, respectively. Furthermore,

$$\boldsymbol{F}_v = \begin{bmatrix} 0 \\ n_x\tau_{xx} + n_y\tau_{xy} + n_z\tau_{xz} \\ n_x\tau_{yx} + n_y\tau_{yy} + n_z\tau_{yz} \\ n_x\tau_{zx} + n_y\tau_{zy} + n_z\tau_{zz} \\ n_x\Theta x + n_y\Theta y + n_z\Theta z \end{bmatrix}, \tag{7}$$

$$\boldsymbol{Q} = \begin{bmatrix} 0 \\ \rho f_{e,x} \\ \rho f_{e,y} \\ \rho f_{e,z} \\ \rho \boldsymbol{f_e} \cdot \vec{U} + \dot{q}_h \end{bmatrix}, \tag{8}$$

Where $\tau_{ij}(i = x, y, z; j = x, y, z)$ represents viscous stress, $\Theta_i(i = x, y, z)$ are terms describing the work of the viscous stresses and of the heat conduction in the fluid, $\boldsymbol{f_e}$ denotes the body force, $f_{e,x}$, $f_{e,y}$, $f_{e,z}$ are the three components of $\boldsymbol{f_e}$, $\dot{q}_h$ is heat fluxes density.

The governing equations were solved by the cell-centered finite-volume method, where the convective terms were computed by the second-order upwind scheme and the viscous flux terms were solved by a central-difference method. The least-squares gradient reconstruction method with the modified Venkatakrishnan gradient reconstruction limiter was used. The equations were integrated in time by a second-order Runge-Kutta method with 20 inner iterations per time step.

2.2 IDDES Method

To include the effect of turbulence, the Improved Delayed Detach-Eddy Simulation [13] was adopted in our simulations. IDDES method is based on the SST k-ω turbulence model [14] with the turbulence length scale in the destruction term D_k of k equation replaced by the IDDES length scale [15].

The k-ω turbulence model reads

$$\frac{\partial \rho k}{\partial t} + \nabla \cdot (\rho \vec{U} k) = \nabla \cdot [(\mu + \sigma_k \mu_t) \nabla k] + P_k - D_k, \tag{9}$$

$$\frac{\partial \rho \omega}{\partial t} + \nabla \cdot (\rho \vec{U} \omega) = \nabla \cdot [(\mu + \sigma_\omega \mu_t) \nabla \omega] + 2(1 - F_1)\rho\sigma_{\omega 2} \frac{\nabla k \cdot \nabla \omega}{\omega} + \alpha \frac{\rho}{\mu_t} P_k - \beta \rho \omega^2, \tag{10}$$

Where k is turbulence kinetic energy, μ is the molecular viscosity coefficient, μ_t is turbulent viscosity, P_k is production term, D_k is diffusion term, ω is turbulent dissipation ratio, $\alpha = \alpha_1 F_1 + \alpha_2(1 - F_1)$, $\alpha_1 = 5/9$, $\alpha_2 = 0.44$, F_1 is Menter blending function, $\beta = 0.075$, $\sigma_k = 0.85$, $\sigma_\omega = 0.85$, $\sigma_{\omega 2} = 0.856$. The IDDES length scale is given by

https://doi.org/10.1017/jmech.2017.45 Published online by Cambridge University Press

$$D_k = \frac{\rho\sqrt{k^3}}{l_{IDDES}}, \tag{11}$$

$$l_{IDDES} = \tilde{f}_d \cdot (1+f_a)\cdot l_{RANS} + (1-\tilde{f}_d)\cdot l_{LES}, \tag{12}$$

$$l_{RANS} = \frac{\sqrt{k}}{C_\mu \omega}, \tag{13}$$

$$l_{LES} = C_{DES}\Delta, \tag{14}$$

$$C_{DES} = F_1 C_{DES1} + (1-F_1)C_{DES2}, \tag{15}$$

$$\Delta = \min\{\max[c_w d_w, c_w h_{\max}, h_{wn}], h_{\max}\}, \tag{16}$$

Where $\tilde{f}_d$, f_a are blending functions, c_μ = 0.09, C_{DES1} = 0.78, C_{DES2} = 0.61, h_{wn} is the grid step in the wall-normal direction, d_w is the distance to the wall, $h_{\max}$ is maximum value of h_{wn}, c_w = 0.15.

Compared to the original DES97 [16] and DDES [17], IDDES inherits their advantages and overcomes several problems such as log-layer mismatch, grid-induced separation and modeled stress depletion.

2.3 SPWVD Method

When the store is launched, the flow inside the cavity is non-periodic and the pressure signals from monitors are non-stationary. Therefore, the traditional Fourier analysis is inadequate and time-frequency analysis technique is required. We considered several time-frequency analysis techniques, such as short-time Fourier transform (STFT), wavelet transform (WV), Wigner-Ville distribution (WVD) and smooth pseudo Winger-Ville distribution (SPWVD). Because of the Gabor limit [18], the time-frequency conglomeration characteristic of the STFT is very poor. WT has a better time-frequency conglomeration characteristic than STFT, but its computational cost is much higher, which renders it impractical for the large number of data in our application. WVD is a powerful alternative for the non-station signals [19]. However, it suffers from cross term badly. SPWVD suppresses the cross-term effects and retains the advantages of WVD in terms of the calculated quantity and accuracy. In this work, we chose the SPWVD method to analyze the non- stationary signals. The formula for SPWVD is as follows [20]:

$$SPWVD_x(t,f) = \int_{-\infty}^{+\infty}\int_{-\infty}^{+\infty} g(\xi)h(\tau)x\left(t+\frac{\tau}{2}\right)x^*\left(t-\frac{\tau}{2}\right)e^{-j2\pi\int_\tau}d\xi d\tau. \tag{17}$$

Where $x(t)$ is sequence signal, $x^*(t)$ is the complex conjugate of $x(t)$, and τ denotes time variable, j is imaginary unit. $g(\xi)$ is time smoothing window function, $h(\tau)$ is frequency smoothing window function, we chose the Gaussian window as both the time and frequency smoothing windows, $g(\xi) = \frac{1}{T}e^{-a\xi}$, $|\xi| < T$, $h(\tau) = \frac{1}{T}e^{-a\tau}$, $|\tau| < T$.

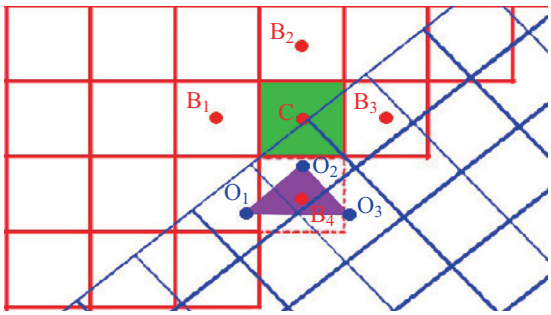


Fig. 1 Overset mesh interpolation schematic.

2.4 Dynamic Chimera Mesh Technique

Dynamic chimera mesh (overset mesh) technique is adopted to account for the large rigid-body displacement of the store. There is a background region enclosing the entire solution domain and one smaller overset region attached to the store. It has been shown good performance in multi-body separation problems as no re-meshing is required [21-24]. Acceptor cells connect the background and the overset regions and couple the solutions on the two overlapping grids through interpolation. A brief introduction of the interpolation method is given as below.

For simplicity, we consider the two-dimensional mesh in Fig. 1. Red mesh is the background mesh and the blue one is the overset mesh. When the variables on the green cell center C are solved, the values from four neighbor cells (B_1 to B_4) are needed. However, those values of acceptor cell B_4 (denoted by dash line) are unknown and need to be interpolated from the donor cells in the overset mesh. To determine the donor cells, we first look for three cells from the overset mesh near the acceptor cell, such as O_1 to O_3, and connect the center of the three cells forming a triangle (marked by pink). If the center of acceptor cell B_4 falls in the triangle, these cells can be used as donor cells, otherwise we continue to try another three cells. Once donor cells are found, we can interpolate the value of donor cells from the overset mesh to acceptor cell by using the shape function. These steps are repeated for each acceptor cell through which the solutions of two overlapping meshes are coupled.

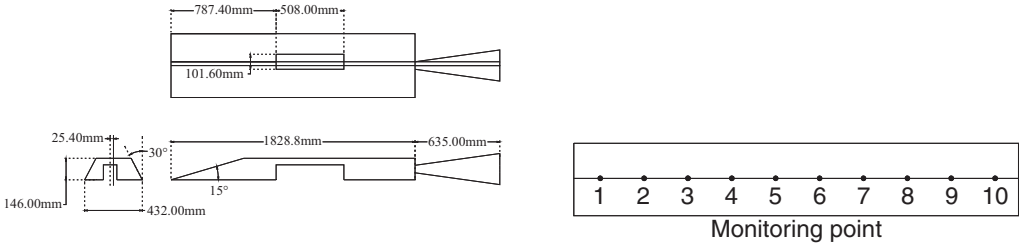
2.5 Validation

2.5.1 Validation Case for Cavity Noise

A widely-used cavity case is considered here to evaluate the accuracy of our numerical method. M219 cavity wind tunnel experiment [25] was conducted by QinetiQ. The cavity has dimensions of L = 0.508 m in length, D = 0.1016 m in depth and W = 0.1016 m in width, giving a ratio of L/D = 5:1, as is shown in Fig. 2. Ten pressure transducers were located on the cavity bottom along the centerline uniformly.

Mesh size inside the cavity is about 1mm. In order to assure y+~1, the thickness of the first layer mesh adjacent to the wall is 2 × 10^{-3} mm. The influence of overset mesh on simulation precision has been consid-

https://doi.org/10.1017/jmech.2017.45 Published online by Cambridge University Press



(a) Sketch of M219 cavity (b) Distribution of monitoring points

Fig. 2 Sketch of M219 cavity and monitoring points distribution.

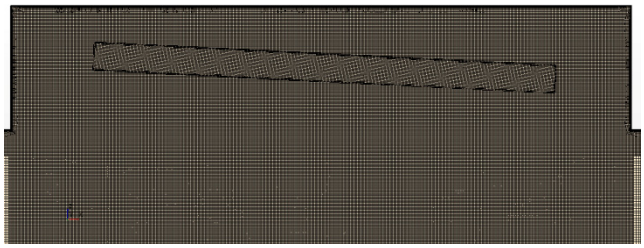
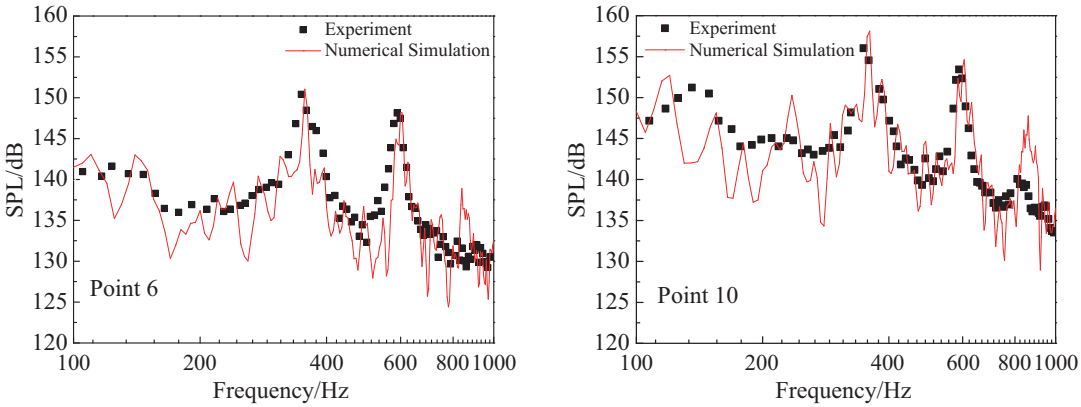


Fig. 3 Grid distribution of M219 cavity.



(a) SPL of monitoring point 6 (x/L=0.55) (b) SPL of monitoring point 10 (x/L=0.95)

Fig. 4 SPL along the center line of cavity bottom.

ered by placing an empty overset mesh region inside the cavity as can be seen in Fig. 3. During the simulation, the empty overset region falls with a constant speed. The simulation was performed with free stream conditions of Ma = 0.85, T = 266.53 K, P = 63000 Pa. The total number of grid cells is 13 million and the simulation time step is 1×10^{-5} s. Total 20000 time steps are computed, which equates to physical time 0.2 s.

For open cavity, we can estimate the cavity mode frequencies by using the semi-empirical formula first proposed by Rossiter [26] and later improved by Heller [27]. The equation is shown as follows:

$$f = \frac{U_\infty}{L} \frac{(m-r)}{M_\infty \left(1+\frac{\gamma-1}{2}M_\infty^2\right)^{-0.5} + \frac{1}{\zeta}}, \tag{18}$$

Where m =1, 2, 3… represents the mode number, r is empirical constant and is equal to 0.38, ζ stands for the ratio of vortex velocity and inflow velocity, U_∞ represents inflow velocity, L is the length of the cavity, M_∞ is the inflow Mach number and γ is the specific heat ratio. Mode frequencies of M219 cavity calculated by the above semi-empirical formula are 148 Hz, 363 Hz and 578 Hz.

Figure 4 shows the sound pressure level results at point 6 and point 10 obtained by Fourier transform method. The solid red curves represent the simulation results while the black dotted curves are experimental results. Close inspection reveals good match among numerical simulation, experiment and the semi-empirical analysis, which demonstrates the reliability and the accuracy of the CFD method in predicting the cavity noise.

Furthermore, we analyzed the pressure data at point 10 by SPWVD method and obtained the energy density $SPWVD_x(t,f)$ (units $Pa^2 \cdot S^{-1} \cdot Hz^{-1}$) in the time-frequency domain as illustrated in Fig. 5. The horizontal axis represents time and the vertical axis is frequency. High energy density indicates high level of noise. We found that the energy density is mainly concentrated at three

https://doi.org/10.1017/jmech.2017.45 Published online by Cambridge University Press

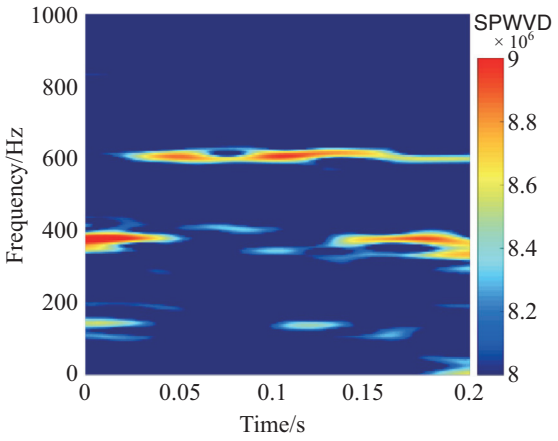


Fig. 5 Energy density time-frequency distributions of point 10.



Fig. 6 Wing/Pylon/Finned-Store configuration.

frequencies corresponding to the first three mode frequencies of the cavity noise. The second and third modes are dominant over the first one as the energy density strengths of second and third modes are bigger than the first. This is in agreement with the Fourier transform result. However, the energy density is not constant for each mode as time grows. From 0 s to 0.04 s, energy density mainly concentrates on the first two modes. After 0.04 s, energy density transfers to the third mode. When t > 0.14 s, it shifts back to the second mode. This is the mode-switching phenomenon discovered by Zhuang [28]. As we can see, the SPWVD method is more powerful because it can obtain more information than the Fourier transform method.

2.5.2 Validation Case for Store Launching

Wing/Pylon/Finned-Store (WPFS) is the standard store separation experiment model, whose CTS data was obtained at Arnold Engineering Development Center (AEDC), and is widely used for validation [29, 30]. Figure 6 shows the geometry of the WPFS model. The store is 3.387 m long, 907 kg in weight and 0.508 m in diameter. Launching method is ejection launch and the inflow Mach number is 0.95.

There are two mesh regions: the background region includes the wing and pylon and the overset region contains the finned-store. To improve the interpolation accuracy, the mesh size ratio between the two regions is less than 1.2. The numbers of grid cells in the overset region and the background region are 5.2 million and 11.5 million respectively.

Figure 7 and Fig. 8 show the results of store displacements and angular orientations from both numerical simulation and experiment. Influenced by the ejection force, the displacement in Y is much larger than those in

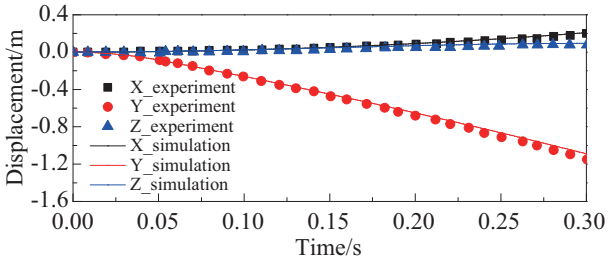


Fig. 7 Displacements of store versus time.

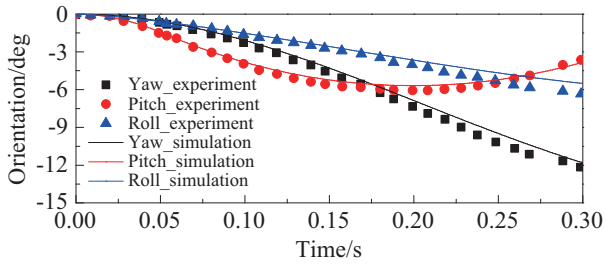


Fig. 8 Angular orientations of store versus time.

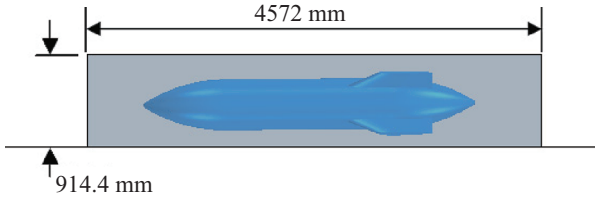


Fig. 9 Simulation model.

other two directions, and the store's pitch angle rises rapidly. After the ejection force vanishes, the pitch angle starts to decrease. It can be observed from the graphs that numerical results are in very good agreement with the wind tunnel test outcomes.

3. COMPUTATIONAL CASE AND ANALYSIS

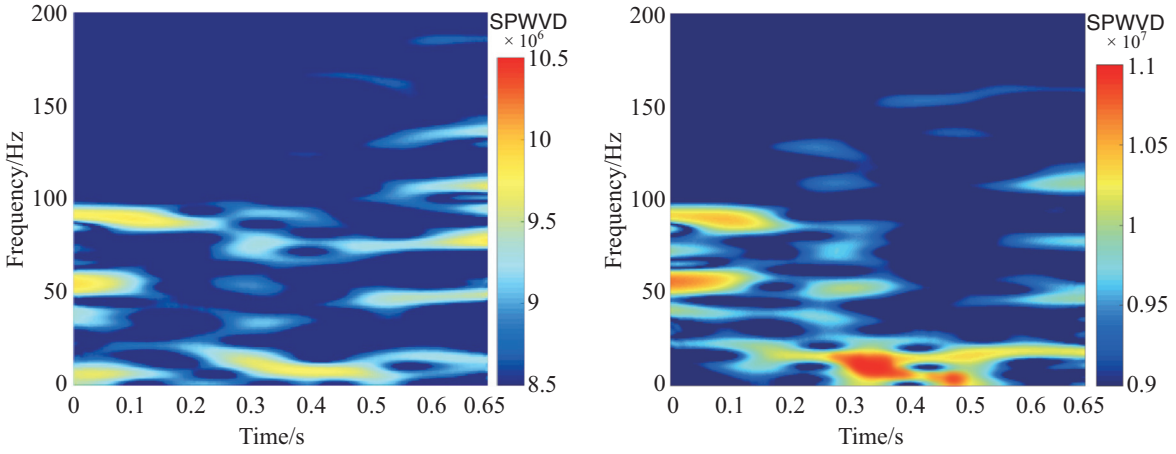
3.1 Simulation Model

To simulate the store launching in the practical conditions, we scale up the M219 cavity with its length equals to 4.572 m while fixing the length-to-depth ratio L/D = 5:1, as is shown in Fig. 9. At the bottom of the cavity ten pressure transducers were set up along the centerline uniformly. Cavity tone frequencies calculated by the semi-empirical formula Eq. (18) are 21 Hz, 53 Hz and 84 Hz. The store we choose is identical to the one used in the WPFS experiment, and launching method remains ejection launch with ejection forces lasting for 0.055 s. Detailed parameters of the store are shown in Table 1. Total mesh number is 27.2 million with 22 million in the background region and 5.2 million in the overset region.

https://doi.org/10.1017/jmech.2017.45 Published online by Cambridge University Press

Table 1 Store parameters

Parameters	Values	Parameters	Values
Reference Length	3.38 m	Transverse moments of inertia Iyy, Izz	488 kg·m^2
Reference Diameter	0.508 m	Forward ejector location	1.24 m (aft of store nose)
Center of mass	1.42 m (aft of store nose)	Forward ejector force	10679.4 N
Mass	907 kg	Aft ejector location	1.75 m (aft of store nose)
Axial moment of inertia Ixx	27 kg·m^2	Aft ejector force	42717.5 N



(a) Point 3 (x/L = 0.25) (b) Point 10 (x/L = 0.95)

Fig. 10 Energy density time-frequency distribution of monitoring points.

The simulation was performed with inflow conditions of Ma = 1.35, T = 223.5 K, angle of attack α = 0°, Reynolds number based on cavity length is Re = 6.9 × 10^7. Inlet boundary condition is set to free stream condition and walls are set to no-slip velocity condition. The time step we choose is 5 × 10^{-5} s and inner step is set to 20 steps to ensure the residuals drop by two orders of magnitude during each time step.

3.2 The Impact of the Store Launching on the Cavity Aero-Acoustics Characteristics

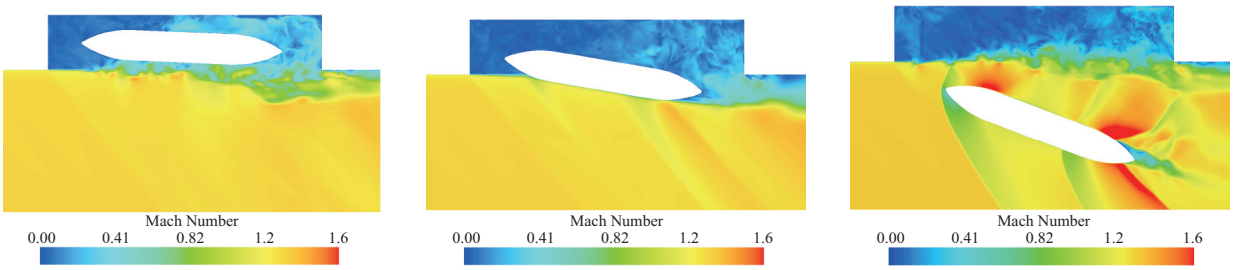
After the unsteady flow field has been established, we continue the simulation for 0.2 s and obtain the cavity aero- acoustic characteristics with the store mounted inside. The store is then released at t = 0.2 s and our simulation continues for another 0.45 s, so the total physical time is 0.65 s. The pressure signals from the monitoring points were analyzed with SPWVD method. Figure 10 shows the energy density time-frequency distribution results at point 3 and point 10 which are located at the front and aft of the cavity respectively.

In Fig. 10, the energy density concentrates for the first 0.2 s on three frequencies corresponding to the first three Rossiter modes. Due to the presence of the store, there are small differences from the results calculated by the semi-empirical formula Eq. (18). Once the store is released at 0.2 s, the aero-acoustic characteristics in the cavity change completely. Both of the results at point 3 and point 10 show that the energy density does not distribute on the Rossiter mode frequencies any more, but shifts into the lower frequency range. The intensity of the energy density at the monitoring point 10 near the trailing edge increases, indicating that the sound pressure level at the back of the cavity boosts due to the store launching process.

Figure 11 shows the instantaneous Mach number contours at the cavity center cross section for different times. Iso-surfaces of Q-criteria [31] for pressure are presented in Fig. 12, which reveal the induced vortex structures. Numerical Schlieren [32] contours are presented in Fig. 13 to highlight the coherence of the shear layer and its breakdown. For t = 0.28 s, the store is still in the cavity. There is an oblique shock wave developed at the leading edge of the cavity. The shear layer loses its stability at 15% along the cavity length, and generates a series of vertexes as can be seen from Fig. 11(a) and Fig. 13(a). Vortex structures inside the cavity are shown in Fig. 12(a).

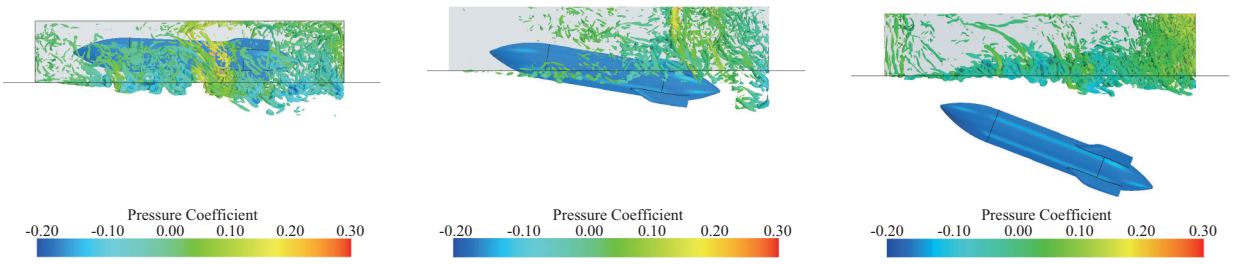
We can see from Fig. 11(b) that at t = 0.37 s the store is falling out of the cavity, and the shear layer is destroyed by the store. As a result, the feedback loop is blocked. Subsequently, the self-sustained oscillation breaks down and the cavity tone vanishes. Meanwhile, because of the disturbance and the volume effect caused by the store falling process, the pressure pulsation am-

https://doi.org/10.1017/jmech.2017.45 Published online by Cambridge University Press



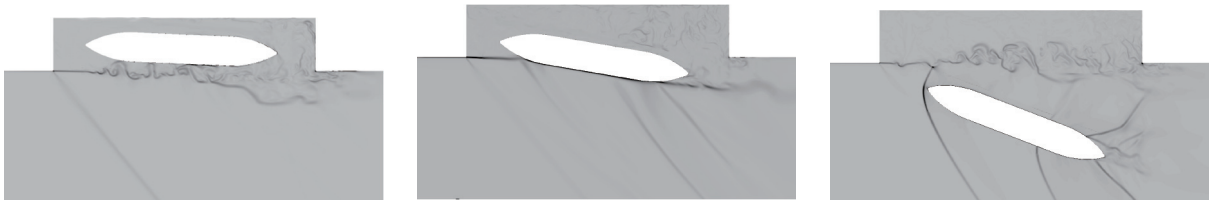
(a) t = 0.28s (b) t = 0.37s (c) t = 0.6s

Fig. 11 Mach number contours of cavity center cross section for different time.



(a) t = 0.28s (b) t = 0.37s (c) t = 0.6s

Fig. 12 Instantaneous iso-surface of Q-criterion (Q = 3e5) for different time.



(a) t = 0.28s (b) t = 0.37s (c) t = 0.6s

Fig. 13 Numerical Schlieren contours of cavity center cross section for different time.

plitude increases and then enhances the unsteadiness of the flow field inside of the cavity, leading to a higher noise level. There are few vortex structures at the front of the cavity while the majority concentrates at the back as is shown in Fig. 12(b) and Fig. 13(b). Therefore, the noise inside of the cavity is non-uniform, where the sound pressure level at the leading edge is weaker than that of the trailing edge.

After t = 0.5 s when the store has fallen out of the cavity completely, the shear layer re-establishes rapidly. The feedback loop is restored along with the self-sustained oscillation. The energy density re-concentrates on Rossiter mode frequencies except that the cavity tone frequencies have changed. There is a new high frequency mode as is shown in Fig. 10. After the store's head falls out of the cavity, an oblique shock wave is formed and interferes with the shear layer as is shown in Fig. 11(c) and Fig. 13(c). It enhances the unsteadiness of the shear layer and intensifies the vortex shedding off from the shear layer, which produces the new high frequency cavity mode.

3.3 The Impact of the Cavity Flow Field on the Store Trajectory

After the internal store is released, it goes through the shear layer. During this process, the store body is subjected to strong unsteady aerodynamic forces, which have great impacts on the trajectories of the store. Figure 14 gives the separation parameters of the store versus time.

Figures 14(a) and (b) show that there are obvious fluctuations in the forces and moments on the store. This is due to the strong unsteady flow field inside of the cavity. The shedding vortexes from the shear layer collide onto the store and change the surface pressure, which results in the irregular distribution of high pressure and low pressure on the store surface.

In the first 0.055 s, the store is dominated by the ejection force and its velocity increases from 0 m/s to -3.5 m/s in a short time as is shown in Fig. 14(c). At the same time, the store is subject to a great upward pitch moment, so the pitch angular velocity increase to 1.3

https://doi.org/10.1017/jmech.2017.45 Published online by Cambridge University Press

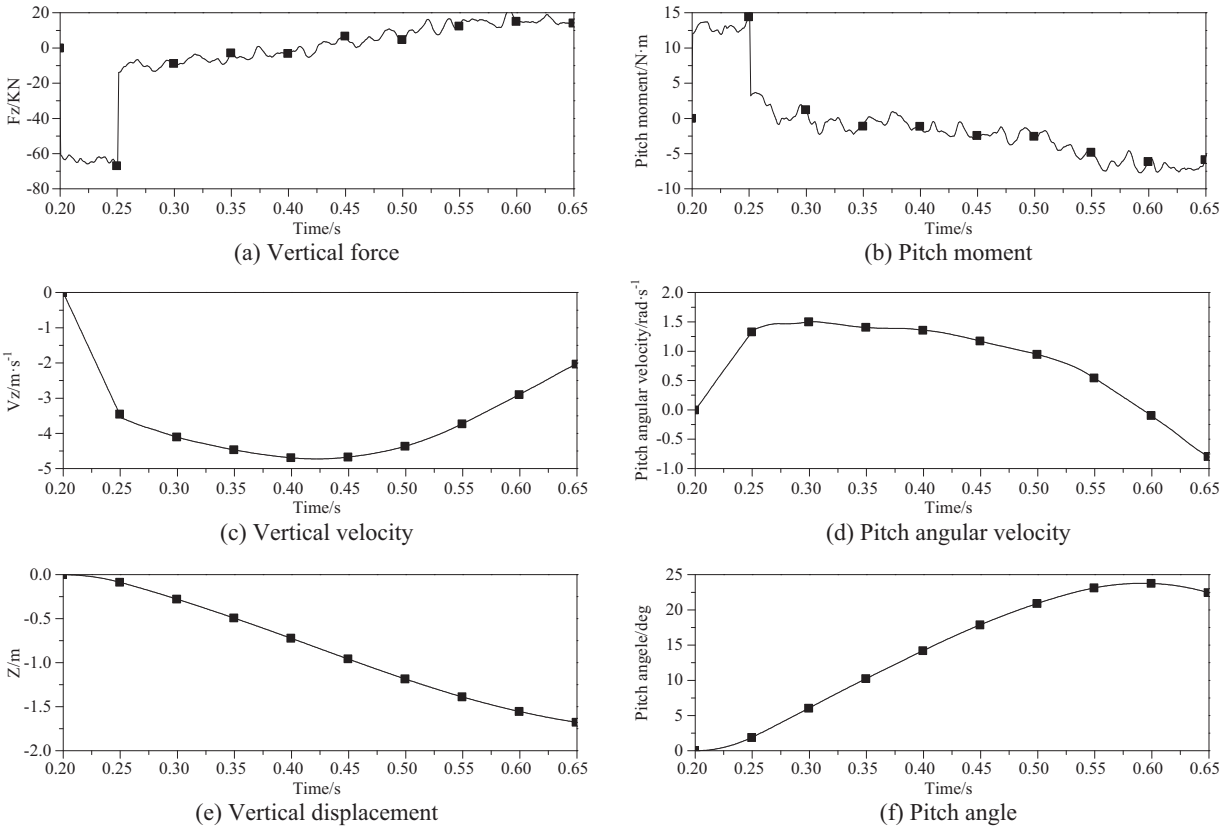
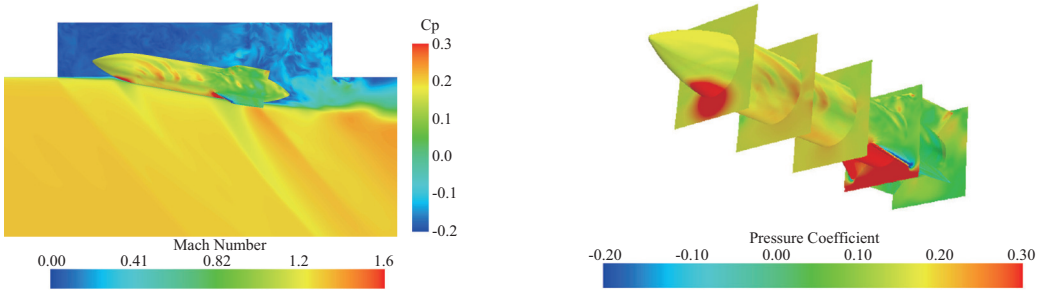


Fig. 14 Separation parameters of store versus time.



(a) Section Mach number contours and body side Cp distribution (b) Pressure coefficient distribution of store

Fig. 15 Mach number contours of the cavity section and pressure coefficient distribution of the store for t = 0.37 s.

rad/s rapidly. Because the ejection force only lasts for a short time, the pitch angle just rises to 1.6 degrees. After 0.255 s, the ejection force stops and the store continues to fall down under the combined force of gravity and the aerodynamic forces. From 0.255 s to 0.32 s, the combined vertical force on the store remains at 10 KN and the falling speed increases steadily with a lower acceleration. From 0.32 s, the store falls through the shear layer where the combined vertical force starts to decrease and eventually reduces to zero at t = 0.43 s. From then on, the direction of the combined vertical force is reverted, which impedes the store separation. The falling speed stops increasing at t = 0.43 s and starts to decrease afterwards.

Figure 15 shows the Mach number contours at the cavity center cross section and the pressure coefficient distribution on the store surface at t = 0.37 s. In Fig. 15(a), the plane is colored by the Mach number and the store is colored by the pressure coefficient. Figure 16 shows the Cp distribution along the symmetric line of the upper and the lower surface of the store. As is shown in Fig. 15, the shear layer is penetrated by the store and collides on its lower surface. An oblique shock forms and pushes pressure built up on the head of the store because a part of the kinetic energy in the shear layer converts to pressure energy. This high-pressure region is centered at x = 0.5 m in Fig. 16 where the pressure coefficient peak is at 0.45. This high-pressure area makes the store subject to a large pitch up moment. At the back of the store, there is an oblique shock due to the fin

https://doi.org/10.1017/jmech.2017.45 Published online by Cambridge University Press

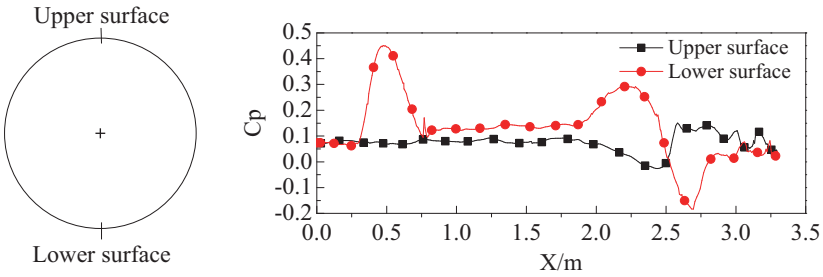


Fig. 16 Pressure coefficient distributions of symmetric line on upper and lower surface for t = 0.37 s.

and a second high-pressure region at x = 2.3 in Fig. 16. This region induces a pitch down moment on the store. A third oblique shock shows up at the tail of the store, which causes the pressure of the lower surface rise at x = 2.8 as can be seen in Fig. 16, however, the pressure of the lower surface of this area is less than the upper surface. Since the influence of the front high-pressure region caused by the shear layer, the combined pitch down moment is very small. Thus, the pitch up angular velocity drops slowly and the store's pitch up angle keeps rising to 24° until t = 0.6 s as is shown in Figs. 14(d) and (f). After that, the pitch angular velocity falls below zero, and the pitch angle starts to decrease.

Figure 16 also shows that the pressure on the lower surface is much higher than that on the upper surface, due to the store's pitch up attitude. As a result, the direction of the vertical aerodynamic force is upward. When the aerodynamic force gets bigger than the gravity, the resultant vertical force will hinder the store from falling as is shown in Fig. 14(c) after t = 0.43 s.

4. CONCLUSIONS

The strong interplay between the cavity and the store during launching under the supersonic inflow condition was studied by using IDDES method. The following conclusions can be drawn from this study.

1. The store launching process has great influence on the cavity aero-acoustic characteristics. When the store falls out of the cavity, the shear layer is destroyed which leads to flow structure changes. The self-sustained oscillation breaks down and the cavity tone vanishes. Main vortexes concentrate at the back of the cavity, so the sound pressure levels increase at the trailing edge of the cavity.

2. After the store has fallen out of the cavity, the shear layer rebuilds quickly and the self-sustained oscillations phenomenon restores. An oblique shock wave is formed at the store's head and interferes with the shear layer, which enhances the unsteadiness of the shear layer and intensifies the vortex shedding from the shear layer. As a result, a new high-frequency cavity mode shows up.

3. Affected by the strong unsteady flow field inside the cavity, the aerodynamic forces and moments on the store fluctuate rapidly. When the store falls through the shear layer, a high-pressure region develops at the head of the store due to the oblique shock and the impact of shear layer. This high-pressure region makes the store's pitch-up angle keeps rising up to 24°. Meanwhile, pitching up leads to large upward aerodynamic forces further impeding the store separation process.

ACKNOWLEDGEMENTS

The work in this paper is supported by the National Nature Science Foundation of China (Grant No. 11172283)

REFERENCES

1. Gai, S. L., Kleine, H. and Neely, A. J., "Supersonic Flow over a Shallow Open Rectangular Cavity," *Journal of Aircraft*, **52**, pp. 609-616 (2014).
2. Beresh, S. J., Wagner, J. L. and Pruett, B. M., "Supersonic Flow over a Finite-Width Rectangular Cavity," *AIAA Journal*, **53**, pp. 296-310 (2014).
3. Handa, T., Miyachi, H. and Kakuno, H., "Modeling of a Feedback Mechanism in Supersonic Deep-Cavity Flows," *AIAA Journal*, **41**, pp. 420-425 (2014).
4. Li, W., Nonomura, T. and Oyama, A., "Feedback Mechanism in Supersonic Laminar Cavity Flows," *AIAA Journal*, **51**, pp. 253-257 (2013).
5. Sun, Y., Zhang, Y. and Taira, K., "Width and Sidewall Effects on High Speed Cavity Flows," *54th AIAA Aerospace Sciences Meeting*, San Diego (2016).
6. Thiemann, C. L., Milne, G. J. and Vakili, A. D., "An Experimental Investigation of Supersonic Cavity Flow Control with Vertical Cylinders," *43rd Fluid Dynamics Conference*, San Diego (2013).
7. Givogue, G., Fowler, W. and Vakili, A., "An Experimental Investigation of 2-D Cylinders Affecting Supersonic Cavity Flow," *29th AIAA Applied Aerodynamics Conference*, Honolulu (2011).
8. Zhang, Y., Sun, Y. and Arora, N., "Suppression of Cavity Oscillations via Three-Dimensional Steady Blowing," *45th AIAA Fluid Dynamics Conference*, Dallas (2015).

https://doi.org/10.1017/jmech.2017.45 Published online by Cambridge University Press

9. Williams, D. R., Cornelius, D. and Rowley, C. W., "Closed Loop Control of Linear Supersonic Cavity Tones," *45th AIAA Fluid Dynamics Conference*, Miami (2007).
10. Thangamani, V. and Kurian, J., "Control of Cavity Oscillations in a Supersonic Flow by Microjet Injection," *Journal of Aircraft*, **50**, pp. 1305-1309 (2013).
11. Robertson, G., Kumar, R. and Doyle, S., "Acoustics of a Supersonic Cavity with a Generic Store," *53rd AIAA Aerospace Sciences Meeting*, Kissimmee, U.S.A. (2015).
12. Blazek, J., *Computational Fluid Dynamics Principles and Applications*, 2nd Edition, Elsevier, London, pp. 16-18 (2005).
13. Shur, M. L., Spalart, P. R. and Strelets, M., "A Hybrid RANS-LES Approach with Delayed-DES and Wall-Modelled LES Capabilities," *International Journal of Heat and Fluid Flow*, **29**, pp. 1638-1649 (2008).
14. Menter, F. R., "Two-Equation Eddy-Viscosity Turbulence Modeling for Engineering Applications," *AIAA Journal,* **32**, pp. 1598-1605 (1994).
15. Strelets, M., "Detached Eddy Simulation of Massively Separated Flows," *39th Aerospace Sciences Meeting and Exhibit*, Reno, U.S.A. (2001).
16. Spalart, P. R., Jou, W. H. and Strelets, M., "Comments on the Feasibility of LES for Wings, and on a Hybrid RANS/LES Approach," *Proceedings of First AFOSR International Conference on DNS/LES*, Ruston, U.S.A. (1997).
17. Spalart, P. R., Deck, S. and Shur, M. L., "A New Version of Detached Eddy Simulation, Resistant to Ambiguous Grid Densities," *Theoretical and Computational Fluid Dynamics*, **20**, pp. 181-195 (2006).
18. Bey, N. Y., "Multi-Resolution Fourier Analysis: Time-Frequency Resolution in Excess of Gabor–Heisenberg Limit," *Signal, Image and Video Processing*, **8**, pp. 765-778 (2014).
19. Xiao, J. and Flandrin, P., "Multitaper Time-Frequency Reassignment for Non-Stationary Spectrum Estimation and Chirp Enhancement," *IEEE Transactions on Signal Processing*, **55,** pp. 2851-2860 (2007).
20. Auger, F. and Flandrin, P., "Improving the Readability of Time Frequency and Time Scale Representations by the Reassignment Method," *IEEE Transactions on Signal Processing*, **43**, pp. 1068-1089 (1995).
21. Hadzic, H., "Development and Application of Finite Volume Method for the Computation of Flows Around Moving Bodies on Unstructured, Overlapping Grids," M. S. Thesis, Department of Fluid Dynamics and Ship Theory, Technische University Harburg, Germany (2006).
22. Steger, J. L. and Dougherty, F. C., "A Chimera Grid Scheme," *Advances in Grid Generation Asme*, **5**, pp. 15-23 (1983).
23. Togashi, F., Ito, Y. and Nakahashi, K., "Overset Unstructured Grids Method for Viscous Flow Computations," *AIAA Journal*, **44**, pp. 1617-1623 (2006).
24. Zhang, L. P., Deng X. G. and Zhang, H. X., "Reviews of Moving Grid Generation Techniques and Numerical Methods for Unsteady Flow," *Advances in Mechanics*, **40**, pp. 424-447 (2010).
25. Henshaw, M. C., "M219 Cavity Case: Verification and Validation Data for Computational Unsteady Aerodynamics," *Technical Report RTO-TR-26*, pp. 453-472 (2002).
26. Rossiter, J. E., "Wind Tunnel Experiments on the Flow over Rectangular Cavities at Subsonic and Transonic Speeds," *Aeronautical Research Council Reports and Memoranda*, No. 3438, Farnborough (1964).
27. Heller, H. H., Holmes, D. G. and Covert, E. E., "Flow Induced Pressure Oscillations in Shallow Cavities," *Journal of Sound and Vibration*, **18**, pp. 535-546 (1971).
28. Zhuang, N. and Alvi, F. S., "Aeroacoustic Properties of Supersonic Cavity Flows and Their Control," *9th AIAA/CEAS Aeroacoustics Conference and Exhibit*, Hilton Head, U.S.A. (2003).
29. Heim, E. R., "CFD Wing/Pylon/Finned Store Mutual Interference Wind Tunnel Experiment," *Arnold Engineering Development Center*, Tennessee (1991).
30. Meakin, R. L., "Multiple-Body Proximate-Flight Simulation Methods," *17th AIAA Computational Fluid Dynamics Conference*, Toronto, Canada (2005).
31. Hunt, H., Wary, A. A. and Moin, P., "Eddies, Streams, and Convergence Zones in Turbulent Flows," *Center for Turbulence Research*, pp. 193-207 (1988).
32. Wu, M. and Martin, M. P., "Direct Numerical Simulation of Supersonic Turbulent Boundary Layer over a Compression Ramp," *AIAA Journal*, **45**, pp. 879-889 (2007).

(Manuscript received December 22, 2016,
accepted for publication May 18, 2017.)

https://doi.org/10.1017/jmech.2017.45 Published online by Cambridge University Press